



# Development of an Electric Arc Furnace Simulation Model Using the Effective Equilibrium Reaction Zone (EERZ) Approach

MARIE-ALINE VAN ENDE<sup>1,2</sup>

1.—Department of Materials Science and Engineering, and Research Institute of Advanced Materials (RIAM), Seoul National University, Seoul 08826, South Korea.  
2.—e-mail: vanende@snu.ac.kr

The development of a kinetic process model for the electric arc furnace (EAF) based on the effective equilibrium reaction zone approach is presented. The model combines kinetic expressions with accurate thermodynamic databases to predict the evolution of the mass, temperature and composition of the scrap, liquid metal, slag and gas phase during the process. The model addresses all the main phenomena occurring during the EAF process using empirical relations linked to process conditions: charge heating by arc and burners, scrap melting, C and O<sub>2</sub> injection, slag-metal-gas reactions and post-combustion. The model can effectively reproduce measured endpoint temperature and composition of the slag and liquid metal in industrial EAF and illustrates the benefits of the hot heel practice. The model serves as a tool to assist in the optimization of the process operation conditions and in the design and evaluation of new process scenarios.

## INTRODUCTION

The electric arc furnace (EAF) is at the heart of the electric steelmaking route for producing steel from recycled scrap metal feedstock. Other iron-bearing feedstock such as direct reduced iron (DRI), hot briquetted iron (HBI), pig iron and hot metal are also charged alone or in combination with scrap in the EAF to meet the demand for high-quality steel.<sup>1</sup> The EAF accounted for about 30% of the global crude steel production in 2019.<sup>2</sup> The importance of the electric steelmaking route is expected to grow further as a result of the urgent need to reduce the CO<sub>2</sub> emissions in the steelmaking industry.

In the EAF process, the iron-bearing material is melted using energy supplied by electrodes and supplemented by oxy-fuel burners and chemical oxidation reactions. The process is divided into four steps:<sup>3</sup> (1) charging of the iron-bearing material mix, flux and sometimes C in the furnace using several buckets (or baskets); (2) melting of the charge (ignition, boring and melting phase); (3) attaining flat bath conditions and refining; (4)

tapping. Slag foaming practice is commonly used in the EAF by the injection of C and O<sub>2</sub> to generate CO(g) in the slag emulsion, causing the slag to foam and shield the electric arc. Impurities in the liquid metal such as P, Mn, C, H, N, etc., are removed through reactions with the gas and slag, which will define the quality of the steel produced at the EAF.

As challenges for the steelmaking industry rise for higher energy efficiencies, lower CO<sub>2</sub> emissions, fluctuating feedstock types and quality and usage of alternative C sources, process modeling is a crucial tool to improve the performance, investigate new strategies and design new operating procedures for the EAF. Several mathematical models of the EAF process have been proposed in literature using diverse approaches.<sup>4–16</sup> A thorough review of these models has been recently published.<sup>17</sup> However, limitations exist in the description of the kinetics and in the thermodynamic description of the phases in the EAF, especially slag emulsion. Accurate thermodynamic description of the phases is needed to determine the heat requirements for heating and melting the EAF charge, the energy released by the chemical reactions and the chemical equilibria among liquid metal, slag and gas phases during the EAF process.

(Received November 29, 2021; accepted January 25, 2022;  
published online February 18, 2022)

The present article describes a comprehensive model for the scrap-based EAF process combining thermodynamic equilibrium calculations and kinetic expressions based on the effective equilibrium reaction zone (EERZ) approach. The model predicts the evolution of the temperature and composition of the liquid metal, slag and gas based on process conditions by covering all the main aspects of the EAF process: energy transfer from arc and burners to the charge, scrap melting and liquid metal heating, slag formation, C and O<sub>2</sub> injection, slag-metal-gas reactions, post-combustion, etc. The model utilizes accurate thermodynamic databases to compute the necessary energy requirements and chemical equilibria between phases. The model predictions are compared with industrial endpoint data to demonstrate their applicability. The model can be easily expanded to include the use of DRI, HBI, pig iron and hot metal as feedstock in the EAF and will be the subject of a future publication.

## MODEL DESCRIPTION

### Effective Equilibrium Reaction Zone (EERZ) Approach

The present kinetic model is developed using the effective equilibrium reaction zone (EERZ) approach.<sup>18</sup> The latter consists of dividing a complex metallurgical process into a finite number of reaction zones in which equilibrium is assumed. The kinetics are considered by varying the size of the reaction zones depending on physical descriptions of the reaction mechanisms, process conditions and the rate of homogenization in the different phases. The size of each reaction zone is described with simplified mathematical functions and empirical relations derived from simulations, experimental studies and plant data. This approach combines the full potential of accurate thermodynamic databases with kinetic parameters in an easy and effective way that can be directly applied to actual plant operation. In addition, the heat generated or absorbed by the chemical reactions at the interface can be directly calculated using the thermodynamic database, enabling accurate heat balance calculations. The EERZ concept was successfully applied to simulate the Rurhstahl-Heraeus (RH) vacuum degassing process,<sup>18</sup> hot metal treatment (powder injection),<sup>19</sup> basic oxygen furnace (BOF) process,<sup>20,21</sup> BOF tapping,<sup>22</sup> mold flux composition changes during the continuous casting process,<sup>23</sup> ladle furnace process,<sup>24–27</sup> tundish<sup>28</sup> and non-metallic inclusion behavior in liquid steel.<sup>29–31</sup>

### Reaction Zones in the EAF Process

The first step in the development of a model using the EERZ approach is to identify the reaction zones in a complex metallurgical process. In the EAF process, reactions between slag (liquid and solid),

liquid metal, scrap, graphite (C), flux, O<sub>2</sub> and off-gas are taking place. The process simulation of the EAF considers the mass and heat balance simultaneously to predict the evolution of the chemistry and temperature of the phases during the process.

The EAF process was divided into ten reaction zones represented in Fig. 1 to consider the main phenomena taking place in the furnace:

- R1: transfer of heat supplied by burners and electrodes to the charge
- R2: scrap melting and dissolution and C dissolution in liquid metal
- R3: oxidation of the liquid metal surface by O<sub>2</sub> from O<sub>2</sub> lance
- R4: dissolution of flux and oxide products from R3 to the slag
- R5: reaction between O<sub>2</sub> and liquid metal at hot spot formed under O<sub>2</sub> lance
- R6: reaction between injected C and liquid slag
- R7: reaction between liquid metal and slag
- R8: homogenization of the liquid metal and heat loss to furnace walls
- R9: post-combustion of the gas, slag homogenization with heat from post-combustion
- R10: heat transfer between liquid metal and slag, and slag discharge

All ten reactions are calculated successively at each time step following the above reaction sequence. Each of these ten reaction zones has a specific kinetic expression linked to process conditions to determine the amount of materials being equilibrated. In the present model, the time step is fixed at 1 min. The following assumptions are made:

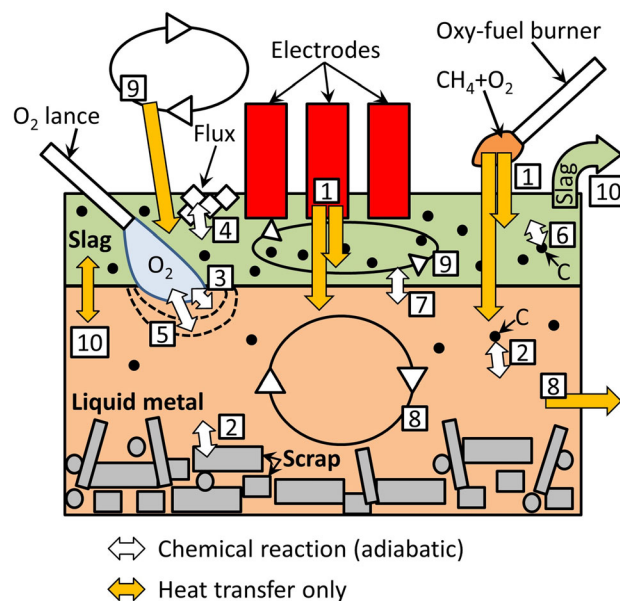


Fig. 1. Schematic diagram of the reaction zones in the present EAF model. The white arrows indicate chemical reactions between the phases (with heat balance), whereas yellow arrows indicate heat transfer only between the phases (Color figure online).

- The liquid metal phase is assumed homogeneous in composition and temperature at the end of each time step (i.e., no temperature or composition gradient in the phase)
- The slag phase is assumed homogeneous in composition and temperature at the end of each time step (i.e., no temperature or composition gradient in the phase). In addition, solids in the slag emulsion (excluding the undissolved fluxes and C) are in equilibrium with the liquid slag
- The effects of slag foaming, dust losses, reactions with refractory and electrodes, and air infiltration in the furnace are not considered
- Moisture, loss on ignition, volatile material, etc., are not considered in the description of the scrap, flux and C materials

The program to perform the EAF simulations is written as a C++ console application to calculate the kinetic expressions and initiate the thermodynamic equilibrium calculations at each reaction zone, to manage the flow of materials between the reaction zones and to iterate the procedure until the end of the metallurgical process. Thermodynamic equilibrium calculations are performed using ChemApp libraries combined with FactSage thermochemical databases (version 8.1).<sup>32</sup> ChemApp<sup>33</sup> is a programming library developed by GTT Technologies (Herzogenrath, Germany) consisting of a rich set of subroutines to perform thermodynamic equilibrium calculations of complex multicomponent, multiphase chemical equilibria and the determination of the associated energy balances. ChemApp is based on the same Gibbs energy minimizer as FactSage. The FactSage commercial databases FactPS, FToxid, FTmisc and FSstel were selected. The solutions FTmisc-FeLQ and FToxid-SlagA were employed to describe the thermodynamic properties of the liquid metal and liquid slag, respectively. Pure solids, solid solutions and gaseous species from the database FactPS and FToxid were selected for the solid oxide phases equilibrated with liquid slag, fluxes, C sources and exhaust gas. The solutions FSstel-FCC\_A1 (FCC Fe), FSstel-BCC\_A2 (BCC Fe) and FSstel-CEME (Cementite Fe<sub>3</sub>C) and pure solids from the FactPS database were used to describe the scrap materials. The C++ program interacts with several Microsoft Excel Worksheets to read simulation input conditions and store calculations results.

### Heat Supplied by Electrodes and Burners to the Charge

The active electrical energy supplied by the electrodes (provided by an external calculation method) and the O<sub>2</sub> and CH<sub>4</sub> flow rates to the oxy-fuel burners are process conditions provided as input to the model. At each time step, the electrical heat,  $Q_{\text{elec}}$  (W = J/s), is transferred to the charge after applying a certain efficiency. The total energy supplied by the oxy-fuel burners,  $Q_{\text{burner-total}}$  (W), is calculated based on the O<sub>2</sub> and CH<sub>4</sub> flowrates at the

given time step and on the flame temperature. The latter is the combusted gas temperature after supplying heat to the charge and the surroundings. In the combustion reaction, it is assumed that the supplied O<sub>2</sub> and CH<sub>4</sub> are completely consumed. The burner efficiency suggested by Logar et al.,<sup>9</sup> which accounts for the decreasing transfer of heat from the burner to the steel with increasing steel temperature, is employed to calculate the heat transferred from the burner to the charge,  $Q_{\text{burner}}$  (W):

$$Q_{\text{burner}} = 0.7 \left( 0.35 + 0.65 \tanh \left( \frac{1300}{T_{\text{ch}}} - 1 \right) \right) Q_{\text{burner,total}} \quad (1)$$

In Eq. (1),  $T_{\text{ch}}$  (°C) is the average scrap temperature when the charge is dominated by scrap and is replaced by the liquid metal temperature when the liquid metal mass is larger than the scrap mass.

After combustion, the gas leaves the furnace without taking part in reactions with the charge. The unused heat affected by the burner efficiency is assumed lost to the surroundings. The electrode efficiency and the flame temperature are model parameters to be adjusted to reproduce the plant data. The sum of the resulting two energy sources  $Q_{\text{elec}}$  and  $Q_{\text{burner}}$  is subsequently distributed between the slag emulsion and the metal charge (scrap or liquid metal) using a model parameter  $D_{\text{slag}}$ . This model parameter should be a function of the slag mass and other properties such as arc length, slag foaming index, conductivity, viscosity, etc. Due to the complexity in determining these properties and their relation with arcing, the parameter  $D_{\text{slag}}$  is simplified to a function of the total mass of the slag emulsion (liquid + solids).

### Scrap Melting

Scrap melting is implemented in the present model using the approach described in the studies of Bekker et al.,<sup>4</sup> MacRosty and Swartz<sup>7</sup> and Logar et al.<sup>9</sup> Their approach consists of allocating the available energy  $Q_{\text{total}}$  (W) between heating the scrap ( $Q_{\text{heating}}$ , W) and melting the scrap ( $Q_{\text{melting}}$ , W) based on the ratio of the scrap temperature ( $T_{\text{sc}}$ , K) to the scrap melting point ( $T_{\text{sc-m}}$ , K).

$$Q_{\text{heating}} = Q_{\text{total}} \left( 1 - \frac{T_{\text{sc}}}{T_{\text{sc-m}}} \right) \quad (2)$$

$$Q_{\text{melting}} = Q_{\text{total}} \left( \frac{T_{\text{sc}}}{T_{\text{sc-m}}} \right) \quad (3)$$

However, in the above studies, the scrap mix was treated as one phase with homogeneous temperature, composition and physical properties. In the present study, this approach was modified to treat individually each scrap material to consider the differences in size and composition that will affect their respective melting behavior. The main factor

influencing the melting behavior of a given scrap is its size and thereby its surface area. As heat is transferred through the scrap surface, the scrap with a larger surface area will take a larger fraction of the available heat than a scrap with smaller surface area. Therefore, the fraction of the available heat  $Q_{\text{total}}$  allocated to each individual scrap material,  $Q_i$  (W), is based on their surface area,  $A_i$  (m<sup>2</sup>).

$$\begin{aligned} Q_i &= \frac{A_i}{A} Q_{\text{total}} \\ A &= \sum_i A_i \end{aligned} \quad (4)$$

where  $A$  is the total surface area of all scrap materials (m<sup>2</sup>). The surface area of the scrap material is calculated based on its equivalent thickness<sup>34</sup>  $L_i$  (m), assuming scrap has a plate geometry:

$$L_i = a_i \left( 1 - 0.13 \frac{a_i}{b_i} - 0.07 \frac{a_i}{c_i} \right) \quad (5)$$

$$A_i = \frac{2W_i}{\rho_i L_i} \quad (6)$$

where  $a_i$ ,  $b_i$  and  $c_i$  are the dimensions of scrap  $i$  ( $a_i < b_i < c_i$ , m),  $W_i$  and  $\rho_i$  the mass (kg) and density (kg/m<sup>3</sup>) of scrap  $i$ , respectively.

Combining Eqs. (2) to (4), we obtain the heat distribution between heating and melting of each scrap  $i$  based on their individual values of  $A_i$ ,  $T_{\text{sc},i}$  and  $T_{\text{sc-m},i}$ :

$$Q_{\text{heating},i} = \frac{A_i}{A} Q_{\text{total}} \left( 1 - \frac{T_{\text{sc},i}}{T_{\text{sc-m},i}} \right) \quad (7)$$

$$Q_{\text{melting},i} = \frac{A_i}{A} Q_{\text{total}} \left( \frac{T_{\text{sc},i}}{T_{\text{sc-m},i}} \right) \quad (8)$$

In the present work, the total energy used to heat and melt the scrap materials,  $Q_{\text{total}}$ , originates from several sources based on the respective amount of scrap and liquid metal in the furnace. When the total mass of scrap is larger than that of liquid metal, the scrap is directly exposed to the arc and burner heat. Therefore, we assume that the energy from the burners and the arc is directly transferred to the scrap. In addition, the liquid metal provides a certain amount of heat to the scrap in contact with it. In this case,  $Q_{\text{total}}$  is equal to:

$$Q_{\text{total}} = (1 - D_{\text{slag}})(Q_{\text{elec}} + Q_{\text{burner}}) + Q_{\text{metal}} \quad (9)$$

The heat transferred from the liquid metal to the scrap charge is calculated based on the equation:

$$Q_{\text{metal}} = hA \frac{W_{\text{metal}}}{W_{\text{scrap}}} (T_{\text{bulk}} - T_{\text{int}}) \quad (10)$$

where  $h$  is the heat transfer coefficient in liquid metal (W/(m<sup>2</sup>K)),  $W_{\text{metal}}$  the mass of liquid metal

(kg),  $W_{\text{scrap}}$  the total mass of scrap (kg),  $T_{\text{bulk}}$  the liquid metal temperature (K) and  $T_{\text{int}}$  the liquidus temperature of the liquid metal at the liquid metal-scrap interface (K). The factor  $W_{\text{metal}}/W_{\text{scrap}}$  provides a correction to the total scrap surface area  $A$  as the latter is not completely exposed to the liquid metal.

When the liquid metal mass is larger than the total mass of scrap, the scrap is partly or entirely submerged in the liquid metal. In this case, it is assumed that the heat from burners and arc in Eq. (9) is transferred to the liquid metal instead of the scrap mix, increasing the value of  $T_{\text{bulk}}$ . The total heat transferred to the scrap mix is therefore given by Eq. (11).

$$Q_{\text{total}} = Q_{\text{metal}} = hA(T_{\text{bulk}} - T_{\text{int}}) \quad (11)$$

It should be noted that, in our approach,  $Q_{\text{metal}}$  is capped to prevent the liquid metal from solidifying in contact with the scrap. The melting point of each scrap  $T_{\text{sc-m},i}$  and the liquidus temperature of the liquid metal  $T_{\text{int}}$  are determined by a thermodynamic equilibrium calculation using FactSage thermodynamic databases. The calculation of  $T_{\text{int}}$  is performed at each time step to consider the changes in the liquid metal composition.

Once  $Q_{\text{total}}$  is determined, it is distributed among all the scrap materials based on their relative surface area (Eq. (4)). The procedure to heat and melt each scrap is represented in Fig. 2. As depicted in Fig. 2a, scrap  $i$ , initially at temperature  $T_{\text{sc},i}$ , is heated using the amount of heat defined in Eq. (7). The sensible heat of all phases constituting scrap  $i$  is considered in the thermodynamic equilibrium calculation to obtain an accurate temperature  $T_{\text{sc},i,\text{new}}$ . Then, we determine the mass of scrap  $i$ , initially at temperature  $T_{\text{sc},i,\text{new}}$ , that can melt based on the amount of heat available for melting defined in Eq. (8) (Fig. 2b). Again, the sensible heat of all phases constituting scrap  $i$  and the heat of fusion is included in the thermodynamic equilibrium calculation to obtain an accurate value of the heat requirements for melting. The remaining, unmelted scrap  $i$  remains at  $T_{\text{sc},i,\text{new}}$ , while the melted part of the scrap at temperature  $T_{\text{sc-m},i}$  will be incorporated adiabatically to the liquid metal pool. The procedure in Fig. 2 is repeated for each scrap individually, so that each scrap may exhibit different temperature  $T_{\text{sc},i,\text{new}}$  and different melting rates based on their respective dimensions and composition. Meanwhile,  $Q_{\text{metal}}$  is extracted from the liquid metal, and, if applicable, the heat from burners and arc is added to the liquid metal.

## O<sub>2</sub> Injection

O<sub>2</sub> is injected via lances to consume the C dissolved in the liquid metal and injected in the slag, to oxidize impurities in liquid metal, to generate FeO to the slag by oxidation of the liquid metal surface and to participate in the post-combustion of

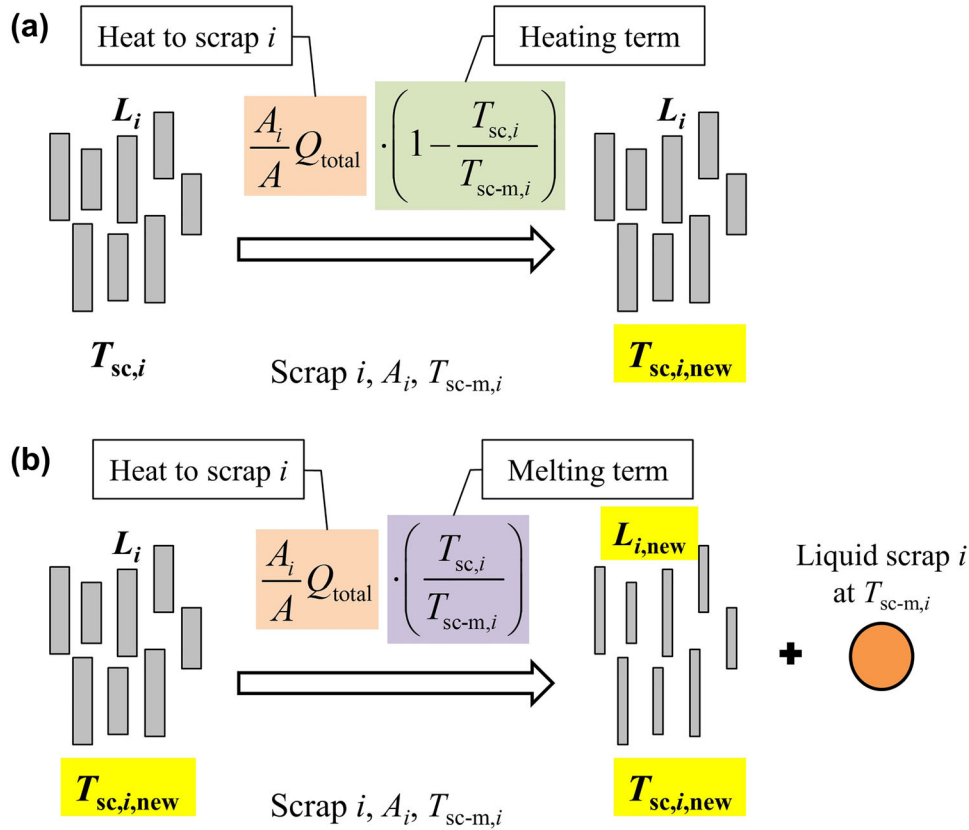


Fig. 2. Schema representing the approach used in the present model for (a) heating and (b) melting a given scrap  $i$ .

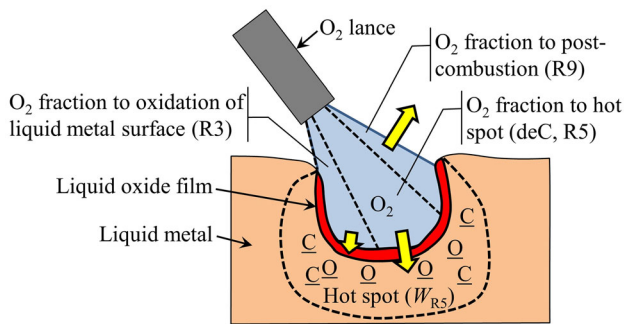


Fig. 3. Schema representing the distribution of  $O_2$  from the  $O_2$  lance between the hot spot (direct deC), liquid metal surface (FeO generation) and post-combustion of the gases.

the off-gases. The division of the injected  $O_2$  among these four reactions will depend on various factors such as the  $O_2$  flow rate, lance position, C availability in the liquid metal and slag, metal bath and slag height, slag foaming, etc. In the present model, oxidation of the injected C is conducted only via the slag FeO for simplification reasons, not directly with the injected  $O_2$ .

In the present model, the injected  $O_2$  can therefore react at three reaction zones, as illustrated in Fig. 3. Model parameters are introduced as fraction of the available  $O_2$  to specify at each time step the distribution of the injected  $O_2$  among the three

reaction sites. These model parameters are adjusted to reproduce the measured C content in liquid metal and FeO content in slag. When sufficient measurement data are available, correlations can be used to assign the value of the model parameters based on the process conditions.

The reactions between injected  $O_2$  and the liquid metal are twofold (Fig. 3). First, at the surface of the liquid metal exposed to  $O_2$ , a film of oxides (mostly FeO) is formed because of the local high  $O_2$  potential (R3 in Fig. 1). The amount of  $O_2$  participating in this reaction is determined by the  $O_2$  distribution model parameter, while the amount of liquid metal exposed to that  $O_2$  is determined based on the stoichiometry of the reaction  $Fe + 0.5 O_2 = FeO$  to maximize the formation of oxides. This reaction is performed adiabatically, generating a lot of heat: the reaction product temperature (gas, liquid metal and slag) exceeds  $2000^\circ C$ . The reacted gas is mixed with the off-gas in R9, the produced liquid slag with the slag in R4, and the unoxidized liquid metal is returned to the liquid metal bath (R3).

Second, a depression (cavity) is generated where the injected  $O_2$  impinges on the liquid metal surface (Fig. 3), creating a hot spot where  $O_2$  and liquid metal are in contact (R5 in Fig. 1). In C-containing liquid metal, decarburization (deC) is the main reaction taking place in the hot spot. In studies of deC by injected  $O_2$ ,<sup>35–37</sup> it is found that the deC rate

depends on the C content of the liquid metal. When the C content is high, the deC rate is generally assumed to be controlled by the  $O_2$  flow rate. When the C content is lower than a critical value—the critical C content—the deC rate decreases drastically and becomes controlled by the mass transfer of C in the liquid metal. In the present study, the following simplified equation is proposed to determine the amount of liquid metal taking part in R5 over the time interval  $\Delta t$  (s),  $\Delta W_{R5}$  (kg):

$$\Delta W_{R5} = \frac{200F_{O_2, \text{hotspot}} M(C) \Delta t}{M(O_2) [\%C_{\text{crit}}]} \quad (12)$$

where  $F_{O_2, \text{hotspot}}$  is the  $O_2$  flow rate dedicated to the hot spot (kg/s),  $M(i)$  the molecular weight of  $i$  (g/mol) and  $[\%C_{\text{crit}}]$  the critical C content (wt%). When the C content in liquid metal is above the critical C content, Eq. (12) ensures that there is sufficient C in the liquid metal to consume  $F_{O_2, \text{hotspot}}$  entirely. On the other hand, when the C content is lower than the critical value, there is more  $O_2$  than the stoichiometric amount required to consume the amount of C in the liquid metal defined in Eq. (12). Hence, the deC rate decreases as a function of  $[\%C_{\text{crit}}]$ . The latter is a model parameter to be adjusted to reproduce the observed C content towards the end of the process.

Lastly, in R9, the unused  $O_2$  is equilibrated adiabatically with the gaseous reaction products from R3 to R8. In this post-combustion reaction, the  $CO(g)$  produced in the previous reaction zones is oxidized to  $CO_2(g)$ . Part of the heat generated by post-combustion is transferred to the liquid slag in R9.

### C Addition and Flux Dissolution in Slag

C is added during the process in different forms. It can be charged as a lump in the bucket together with Fe sources and other additives or directly via a hopper or injected as a powder through a lance or injectors. The main purpose of C injection is slag foaming, which improves the energy efficiency, burry the arc and protect the furnace shell. Charge C is also added as carburizer for the liquid metal, providing chemical heating and contributing to slag foaming. Slag foaming occurs when the C reacts with  $O_2$  and/or FeO from the slag to produce  $CO(g)$ .

In the present model, the oxidation of the injected C is simplified to consider only the oxidation by slag, not directly by  $O_2$ . The C material can therefore react (i) with the slag (FeO) (R6 in Fig. 1) or (ii) dissolve in the liquid metal (R2 in Fig. 1). Depending on the type of C, its addition time and method (bucket, hopper or injection), its reactivity and other surface properties, the distribution of C between the two reaction sites will differ. In the present model, the releasing rate (i.e., the amount of C released in slag and liquid metal per min) and the distribution of each C material between the two sites is assigned

by model parameters adjusted to reproduce the composition of the liquid metal and slag. At each time step, equilibrium calculations at the two possible reaction zones are performed as follows:

- (i) In the case of the reaction between the C particle and the slag (R6), it is expected that only a certain amount of liquid slag surrounding the C particle and only the outer part of the C particle are taking part in the reaction, as illustrated in Fig. 4. Two model parameters are therefore introduced to define the ratio of liquid slag to C and the reaction rate of the released C in the slag. Gaseous products of the reaction are mixed with the off-gases and participate in the post-combustion reaction (R9). The reaction between the defined amount of C and liquid slag is performed adiabatically. The metal produced by the reduction of slag components by C (mostly Fe) is returned adiabatically to the liquid metal bath. The remaining unreacted C stays in the slag for several time steps until it is completely consumed or discharged with a fraction of the slag (R10).
- (ii) In the case of C dissolution in liquid metal (R2), it is assumed that, once released in the liquid metal, the designated amount of C (based on the reaction rate and distribution) dissolves readily in the entire liquid metal bath. Adiabatic conditions are employed in the equilibrium calculation.

The ash components of the C materials, consisting mainly of metal oxides ( $CaO$ ,  $Al_2O_3$ ,  $SiO_2$ ,  $FeO$ ,  $MnO$ ,  $MgO$ ,  $TiO_2$ ,  $P_2O_5$ ,  $V_2O_5$ ,  $Cr_2O_3$  and S), are included in the description of the C materials. They participate in the two reaction zones and, along with all other oxide products of the reactions, are eventually mixed adiabatically with the slag in R9.

Flux dissolution in the slag emulsion is approached using a model parameter defining the dissolution rate of each flux (kg/min). The latter is estimated based on the process and slag conditions at the time of addition. At each time step, the

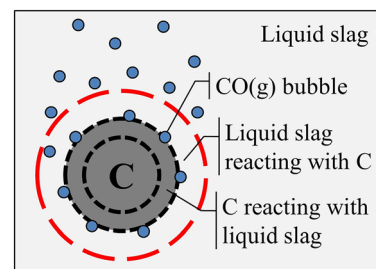


Fig. 4. Schema representing the reaction between injected C and liquid slag with the subsequent formation of  $CO(g)$  bubbles contributing to slag foaming. The red dashed circle in the liquid slag represents the mass of slag surrounding the C particle that will take part in the reaction, while the outer part of the C particle delimited by black dotted circles indicates the mass of C that will take part in the reaction with the liquid slag (Color figure online).

determined amount of flux is equilibrated adiabatically with the entire slag (liquid + solids) in R4.

### Reaction at the Slag/Metal Interface

The reaction between slag and liquid metal in the EAF process (R7 in Fig. 1) governs the removal of impurities such as Si, P, etc., from the liquid metal to the slag. The kinetics of the reaction at the slag/metal interface are expressed using mass transfer rate coefficients in liquid metal,  $k_m$  (1/s), and in slag,  $k_s$  (1/s). In gas-stirred ladles, the mass transfer rate coefficients are mostly governed by the mixing intensity in the steel bath, for which an expression is derived using the mixing energy.<sup>24,38–40</sup> However, an expression of the mixing energy is not readily available for the EAF. Therefore, in the present study, the mass transfer coefficients in liquid metal and slag are evaluated based on the process conditions and on the impurity removal from the liquid metal (Si, Mn, P, etc.) by slag during the process. The mass of liquid metal,  $\Delta W_{R7,m}$  (kg), and that of liquid slag,  $\Delta W_{R7,s}$  (kg), taking part in the slag/metal reaction during the time interval  $\Delta t$  (s) are expressed as follows:

$$\Delta W_{R7,m} = k_m W_{\text{metal}} \Delta t \quad (13)$$

$$\Delta W_{R7,s} = k_s W_{\text{slag}} \Delta t \quad (14)$$

where  $W_{\text{slag}}$  is the mass of liquid slag in the EAF (kg). Like all reactions in the model, the equilibrium calculation is performed under adiabatic conditions. Only the liquid slag takes part in the slag/metal reaction (no solids) and no gas can form (i.e., no deC is allowed). The metal products of the reaction are homogenized with the liquid metal at R8, while the oxide reaction products are mixed with the slag in R9.

### Homogenization and Heat Transfer Between Slag and Liquid Metal, Slag Discharge

The metallic products of reaction zones R3, R5, R6 and R7 are equilibrated adiabatically with the remaining liquid metal at reaction zone 8. Heat loss from the surroundings is also extracted from the liquid metal in this reaction zone. The heat loss is estimated to reproduce the liquid metal temperature measurements.

As mentioned earlier, gaseous products from all reaction zones, except the gas produced by the oxy-fuel burners in R1, are equilibrated adiabatically with the unused lance  $O_2$  at reaction zone R9. This post-combustion reaction produces heat that is transferred to the slag emulsion. The amount of heat is determined by a model parameter fixing the temperature drop of the gas after post-combustion. All the liquid and solid oxide products from reaction zones R3 to R7 are equilibrated with the unreacted slag. If available, the heat provided by the post-combustion reaction is included in the reaction.

After the homogenization reactions, the slag emulsion and the liquid metal are usually at different temperatures, which may trigger a heat transfer between the two phases (R10 in Fig. 1). The heat transferred between the slag and the liquid metal,  $Q_{\text{slag-metal}}$  (W), is estimated with this relation:

$$Q_{\text{slag-metal}} = h_{sm} W_{\text{slag}} (T_{\text{slag}} - T_{\text{metal}}) \quad (15)$$

where  $h_{sm}$  is the heat transfer coefficient between the slag and liquid metal (W/(kgK)).

Toward the end of the process, the slag is discharged through the slag door prior to the liquid metal tapping or when the slag height is excessive during the process. It should be noted that the exact amount of slag discharged cannot be measured during plant operation. Hence, an evaluated value is used in the simulation. Assuming that the slag phase is homogeneous, solid phases, undissolved fluxes and unreacted C remaining in the slag emulsion are discharged from the furnace with the liquid slag according to their mass fraction in the emulsion.

## SIMULATION RESULTS AND DISCUSSION

The model was validated using industrial EAF operation data and measurements provided by companies from the steelmaking consortium led by Prof. In-Ho Jung at Seoul National University, Republic of Korea.<sup>25</sup> As process details cannot be provided here, an example of a heat published in the literature by Logar et al.<sup>9,10</sup> is used to illustrate the applicability and appropriateness of the model. In these publications, details of real plant operations and plant endpoint measurements based on 40 different heats are provided and employed in the present study. The process operation data related to gas flow rates at burners and lances, electrode energy and heat loss (determined for the present model) are depicted in Fig. 5a. Figure 5b shows the feeding rate of dolomite and lime, injection rate of C and slag discharge rate. The composition of the input materials for the present simulation is listed in Table I. In the EAF operation described by Logar et al.,<sup>9,10</sup> 85 tons of scrap is charged in three buckets. An overall scrap composition is provided (Table I), but no information could be found on the dimensions and distribution of different types of scraps in the buckets. To illustrate the influence of the scrap size on their melting behavior, a mixture of two scraps with different dimensions was chosen in the present simulation (Table I), although both scraps have identical composition. The combustible components in the scrap ( $\sim 1.1$  wt%) are not included in the present model. The amounts of dolomite and lime were evaluated to match the CaO/SiO<sub>2</sub> ratio and MgO content in the slag measured at endpoint.

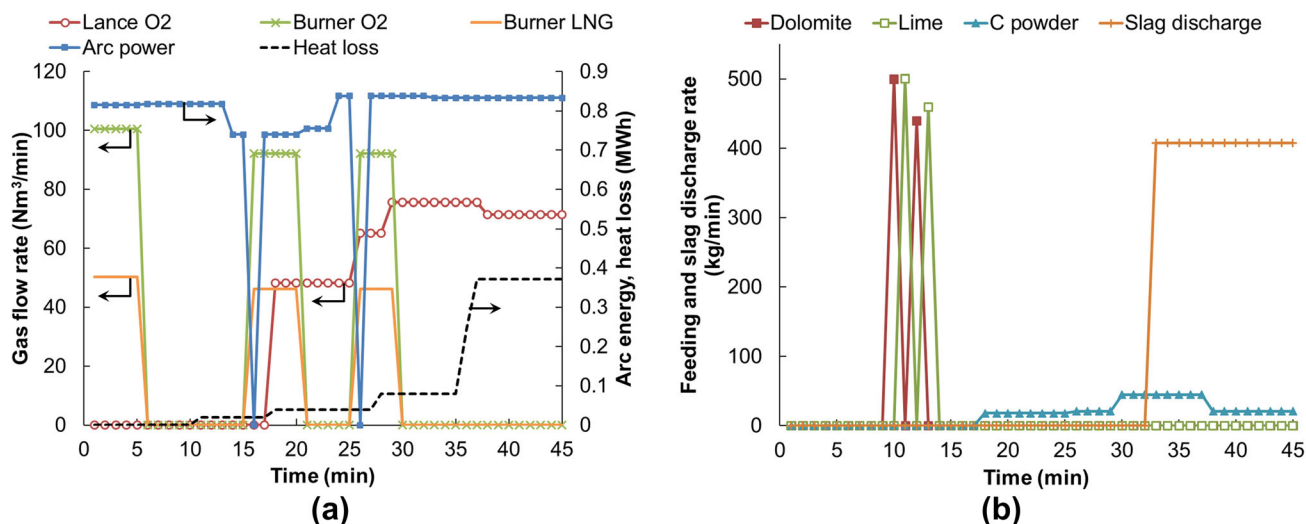


Fig. 5. Evolution of (a) the gas flow rates at oxy-fuel burners and O<sub>2</sub> lance, electrode energy, applied heat loss and (b) material feeding rates and slag discharge rate used as input simulation conditions in the present simulation.

The model parameters employed in the simulation are listed in Table II. Most of these values are evaluated to reproduce the measured endpoint chemistry of the liquid metal and slag as well as the measured endpoint temperature. As the electrode efficiency cannot be easily evaluated by the present authors, its value is set as 100%. The flame temperature at the oxy-fuel burners (Table II), heat loss (Fig. 5a) and post-combustion gas temperature (Table II) are adjusted to reproduce the measured endpoint temperature. The evolution of the heat loss, which is extracted from the liquid metal in the present model, follows the general energy loss in liquid steel calculated by Logar et al.<sup>9</sup> They observed a greater loss of energy occurring to the liquid steel during flat-bath conditions. The value of the heat transfer coefficient in liquid metal was fixed at 10,000 W/(m<sup>2</sup> K), which is consistent with the values estimated in the studies by Opitz and Treffinger<sup>11</sup> and Li et al.<sup>41</sup>

Figure 6 depicts the evolution of the composition of the liquid metal during the course of the EAF treatment calculated with the present model. The measured endpoint contents, which are average values of about 40 heats, are indicated by solid markers. The standard deviations of the measured endpoint values are specified with error bars. During the first 17 min of the process, the composition of the liquid metal is constant and identical to that of the scrap (Fig. 6(a)). In that period, the slag is composed mainly of solid CaO and solid MgO originating from the fluxes added in the first bucket. Based on the given process conditions, there is no possibility of a liquid slag formation with the added fluxes until the start of O<sub>2</sub> blowing. Therefore, no liquid metal refining reaction can take place in that period. From the 18th min after the start or arcing, O<sub>2</sub> is injected in the charge along with C (Fig. 5). As a result, oxidation of the liquid metal is initiated. It

is clear from Fig. 6a that the first element to be oxidized is Si. The low temperature conditions and low C content in liquid metal have favored this reaction over the oxidation of C. The fast Si oxidation rate is maintained until the Si content reaches about 0.1 wt%, after which it slows down. The liquid Mn is also gradually oxidized, but at a slower rate than Si. At about 40 min, oxidation of Mn slows down, giving a predicted final Mn content of 0.43 wt%, which is in good agreement with the endpoint measurement. Oxidation of C from the liquid metal starts at about 27 min. The deC rate is rather constant until the end of the heat. At endpoint, the calculated C content is ~670 ppm, which is consistent with the measured endpoint value of 600 ± 90 ppm. The Cr content in liquid metal remains rather constant during the heat, although slight oxidation can be noticed after about 30 min, bringing down the Cr content to ~0.157 wt%. The latter concurs with the average measured Cr endpoint. Figure 6b provides a detailed view of the calculated P content during the heat as well as the Si content toward the end of the EAF. At about 30 min, the removal of P from the liquid metal begins. The removal rate of that element is quite high. Within 10 min, the P content dropped from ~500 ppm down to ~85 ppm. After a fast oxidation of P, the P removal slows down when P content reaches ~100 ppm. During the last few minutes of the process, the P content is rather stable at about 85 ppm, with a slight tendency to increase. The Si content continues to decrease until the end of the heat and reaches about 100 ppm at endpoint. As seen in Fig. 6a and b, the calculated endpoint composition of the liquid metal is in very good agreement with the measurements.

The evolution of the liquid metal and slag temperature predicted by the model is presented in Fig. 7 along with the endpoint measurement of the



**Table I. Composition of input materials, scrap dimensions and bucket content and charging time for the EAF simulation**

<b>Flux and C composition (wt%)</b>						
	<u>CaO</u>	<u>Al<sub>2</sub>O<sub>3</sub></u>	<u>SiO<sub>2</sub></u>	<u>MgO</u>	<u>C</u>	
Dolomite	57.24	0.45	0.71	40.6	-	
Lime	100	-	-	-	-	
C	-	-	-	-	100	

<b>Scrap composition (wt%) and dimensions (length × width × thickness, m)</b>							
	<u>Fe</u>	<u>C</u>	<u>Cr</u>	<u>Mn</u>	<u>P</u>	<u>Si</u>	<u>dimensions</u>
Scrap 1	98.05	0.35	0.19	0.79	0.05	0.57	0.4 × 0.15 × 0.15
Scrap 2	98.05	0.35	0.19	0.79	0.05	0.57	0.1 × 0.1 × 0.1

<b>Bucket content (ton) and charging time (min)</b>					
	<u>Scrap 1</u>	<u>Scrap 2</u>	<u>Dolomite</u>	<u>Lime</u>	<u>Charging time</u>
Bucket 1	20	20	1	1	0
Bucket 2	15	10	-	-	15
Bucket 3	20	-	-	-	25

**Table II. Model parameters used in the present simulation.  $W_{\text{slag total}}$  is the mass of total slag including liquid and solids (kg)**

<u>Model parameter</u>	<u>Value</u>	<u>Units</u>
Dissolution rate of lime, dolomite and C	100	kg/min
Reaction rate of injected C (all reacting with slag)	20	kg/min
Ratio slag to C reacting with slag	30	-
Arc (electrode) efficiency	100	%
Flame temperature (LNG)	1500	°C
Fraction of arc and burner energy to slag ( $D_{\text{slag}}$ )	$3.33 \cdot 10^{-5} W_{\text{slag total}}$	-
O <sub>2</sub> usage	17–22	%
To hot spot (direct deC)	55–60	%
To surface (FeO formation)	0.1	wt%
Critical carbon content [%C <sub>crit</sub> ]	100	°C
$\Delta T$ post combustion	0.001–0.005	s <sup>-1</sup>
Mass transfer rate coefficient in metal $k_m$	0.001–0.006	s <sup>-1</sup>
Mass transfer rate coefficient in slag $k_s$	10,000	W/(m <sup>2</sup> K)
Heat transfer coefficient in liquid metal $h$	15	W/(kgK)
Heat transfer coefficient between slag and metal $h_{\text{sm}}$		

liquid metal (with the reported standard deviation). It should be noted that the temperature shown in this graph represents the overall liquid metal temperature, assuming that the entire liquid metal is homogeneous at the end of each time step. In addition, solidification of the liquid metal is not considered in the model. That is, in the simulations, the liquid metal remains always in liquid state even when the calculated liquid metal temperature falls below its liquidus or solidus temperature. As seen in Fig. 7, the absence of hot heel and residual slag in the furnace at the beginning of the heat renders the

melting process rather slow and difficult. During the first 10 min of the heat, the predicted temperature of the liquid metal and slag is well below 1400 °C. That is, part of the liquid metal has solidified again when coming in contact with cold fluxes and the furnace lining below. Although the predicted temperature is below the solidus of the liquid metal, it does not necessarily mean that the entire liquid metal has solidified. As mentioned above, this temperature represents the overall average temperature of the liquid metal pool. In reality, large temperature variations may exist within the liquid

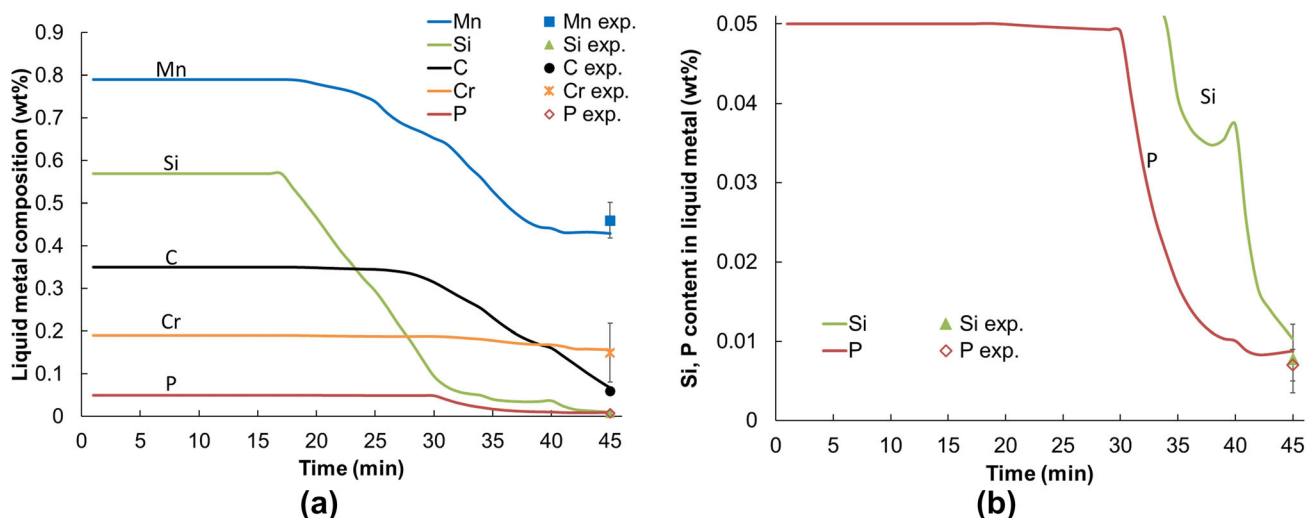


Fig. 6. (a) Calculated concentration profile of Mn, Si, C, Cr and P in liquid metal during the EAF process along with endpoint measurements; (b) detailed view of the calculated P and Si concentration profiles in the liquid metal.

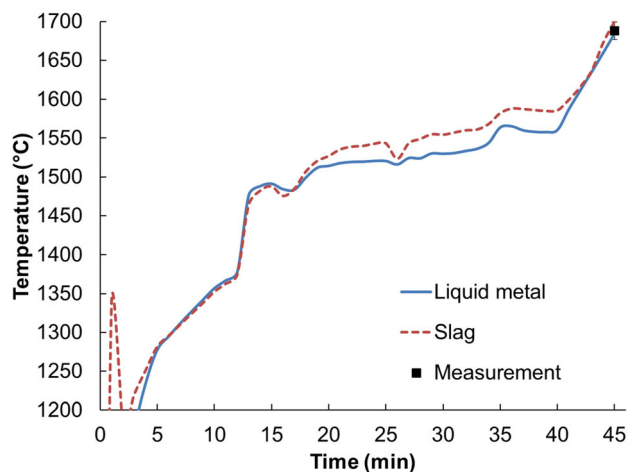


Fig. 7. Calculated temperature profile of the liquid metal and slag emulsion during the EAF process along with measured endpoint temperature.

metal pool, especially at that period of the heat. However, such low predicted temperature suggests that a large part of the liquid metal may have re-solidified. It takes more than 10 min for the charge to reach overall temperatures  $> 1400$  °C. During the  $O_2$  and C injection period starting at 18 min, the liquid metal and slag temperature increases slowly from 1500 to 1560 °C. The scrap melts intensively during that period and consumes the liquid metal superheat. Therefore, the liquid metal temperature hovers a few degrees above its melting temperature. The slag temperature is higher than the liquid metal owing to the exothermic oxidation of the injected C and liquid metal occurring in the slag. At 40 min into the process, the charge temperature increases significantly. It marks the end of scrap melting, after which large amount of heat is not consumed by scrap melting anymore. The endpoint

temperature of the liquid metal obtained with the simulation is 1684.4°C, which is in good agreement with the measured endpoint of  $1688 \pm 11$  °C.

The melting behavior of the scrap charged during the process calculated with the present model is shown in Fig. 8. As Fig. 8a shows, the mass of liquid metal increases continuously for 40 min. The scrap in the first bucket melts progressively: slowly at first, then at an increased rate. Figure 8b depicts the melting behavior of each scrap individually. Due to its smaller dimensions, scrap 2 in the first bucket melts much faster than scrap 1. When the second bucket is charged, about 10 tons of scrap 1 from the first bucket remained in the furnace. The melting continues with the remaining scrap 1 and the fresh scrap from the second bucket. At the third bucket charging, about 16 ton of scrap from the second bucket remained. The charged scrap is entirely melted within 40 min. The simulated scrap melting progression is in good agreement with that obtained by Opitz and Treffinger<sup>11</sup> while using an average scrap diameter of 0.125 m and a heat transfer coefficient in liquid metal of 9000 W/(m<sup>2</sup> K). It should be noted that the melting behavior of the scrap will vary with the scrap dimensions and the value of the heat transfer coefficient in liquid metal. While a constant value was used in the present study, a better expression for the heat transfer coefficient should be used to consider the effect of stronger mixing conditions during  $O_2$ -C injection and slag foaming.

The evolution of the phases constituting the slag emulsion during the EAF process calculated with the current model is depicted in Fig. 9a. As no residual slag is present in the furnace and no  $O_2$  is blown at the beginning of the process, only solid CaO and solid MgO originating from the lime and dolomite fluxes are present in the slag emulsion. Their respective amount increases linearly owing to

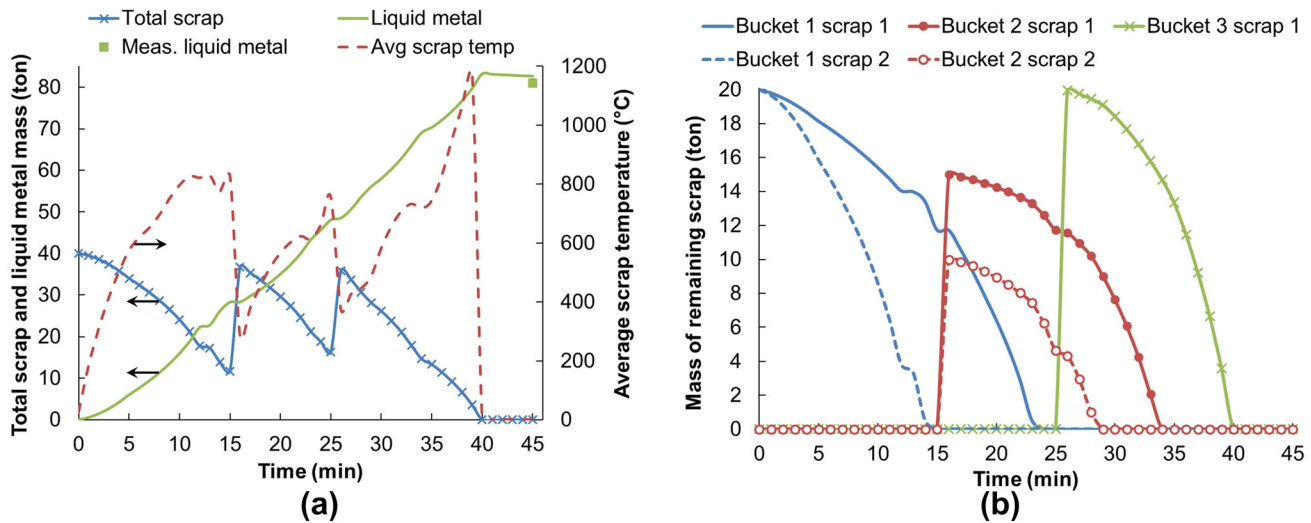


Fig. 8. Evolution of (a) the total mass of scrap and liquid metal and average scrap temperature and (b) the mass of each scrap individually during the EAF process calculated with the present model.

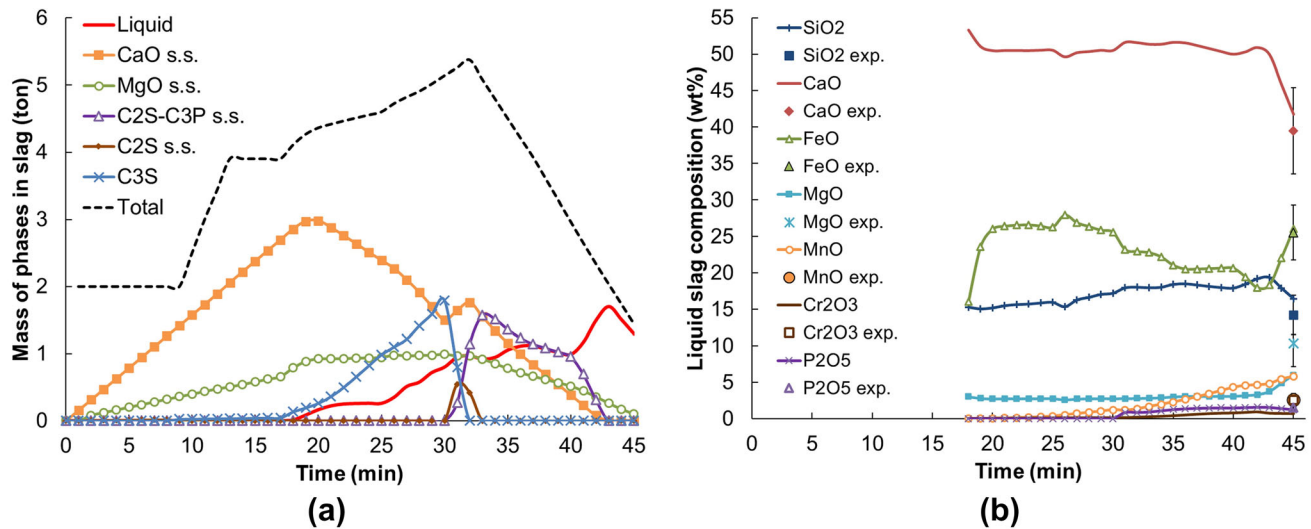


Fig. 9. Evolution of (a) the mass of the phases in the slag emulsion and (b) the composition of the liquid slag calculated with the current model along with the measured endpoint slag composition (s.s. = solid solution, C2S =  $\text{Ca}_2\text{SiO}_4$ , C3P =  $\text{Ca}_3\text{P}_2\text{O}_8$ , C3S =  $\text{Ca}_3\text{SiO}_5$ ).

their constant dissolution rate (Table II). Once  $\text{O}_2$  injection is initiated at the 18th min, a large amount of  $\text{SiO}_2$  generated by the oxidation of Si from the liquid metal (Fig. 6a) and a large amount of FeO from the oxidation of the liquid metal surface (R3) accumulate in the slag emulsion, leading to the formation of solid  $\text{Ca}_3\text{SiO}_5$  (C3S) and liquid slag. The mass of these two phases increases continuously as  $\text{SiO}_2$  and FeO are continuously generated and solid CaO dissolves in these phases.

The calculated composition of the liquid slag is provided in Fig. 9b along with the slag endpoint measurement (with the reported standard deviation). The CaO content in liquid slag is about 50 wt% (CaO saturated conditions), and the FeO and  $\text{SiO}_2$  contents are in the 25 and 15 wt% range, respectively. At about 30 min, solid C3S

transitioned to the solid solutions  $\text{Ca}_2\text{SiO}_4$  (C2S) and  $\text{Ca}_2\text{SiO}_4\text{-Ca}_3\text{P}_2\text{O}_8$  (C2S-C3P). C2S-C3P is an important solid solution in dephosphorization of liquid steel as it can dissolve a large amount of  $\text{P}_2\text{O}_5$ <sup>42,43</sup>. As seen in Fig. 6b, the removal of P from the liquid metal is significantly increased when the C2S solid solution becomes stable. The CaO content in the liquid slag (Fig. 9b) remains stable at about 50 wt%. On the other hand, the  $\text{SiO}_2$  and MnO content in liquid slag increases at the expense of FeO, which drops down to about 20 wt%. The total amount of phases in slag increases and reaches a maximum of 5.4 tons at 32 min (Fig. 9a), after which it steadily decreases as the slag is gradually discharged from the furnace (Fig. 5b). The fraction of liquid slag increases sharply during the last minutes of the heat as the slag temperature increases

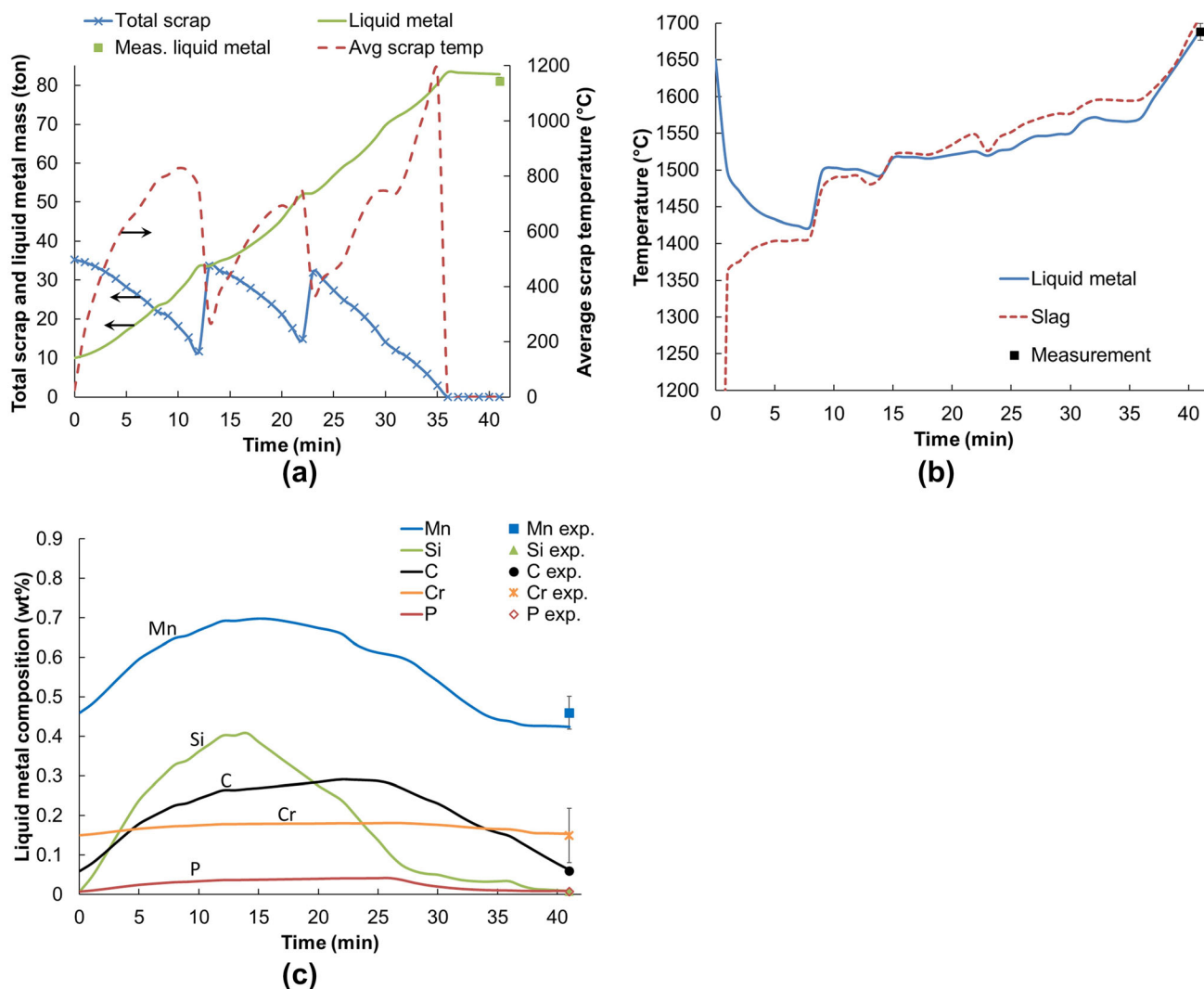


Fig. 10. Evolution of (a) the total mass of scrap and liquid metal and average scrap temperature, (b) the temperature profile of the liquid metal and slag and (c) the liquid metal composition calculated with the current model for the modified EAF process employing 10 tons hot heel.

rapidly (Fig. 7). At endpoint, the slag contains about 1.3 tons of liquid slag and 100 kg of MgO solid solution (62 wt% MgO). The FeO content in the liquid slag increases sharply toward the end as the mass of slag is low and the oxidizable elements in liquid metal become scarce. As observed in Fig. 9b, the agreement between the calculated and measured endpoint slag composition is good. The calculated MgO content is lower than the measurement, probably because the slag sampled at the plant contains some solids. When including the MgO solid solution in the overall slag composition, the calculated MgO content reaches ~10 wt%.

As exhibited in Figs. 6, 7, 8 and 9, the model can successfully reproduce the endpoint measurements using the industrial process conditions. The present model was further validated with industrial data from several other companies. Once validated, the model can be used to explore new process scenarios to improve and optimize the operating procedures.

In modern EAF operation, a hot heel practice is usually employed as it provides several benefits<sup>6</sup>: earlier O<sub>2</sub> blowing and slag foaming, increased arc stability, reduction of power-on-time, lower energy consumption, etc. The hot heel size varies between 10 to 20% of the actual heat size. The effect of employing a hot heel practice in the above EAF process is illustrated in Fig. 10. Ten tons of hot heel at 1650 °C with composition identical to the production metal was used in the simulation. The mass of each scrap was decreased equally in each bucket to amount to 75 tons in total. As seen in Fig. 10a, owing to the lower scrap amount in the bucket and the presence of liquid metal in the furnace, the scrap is melting faster, which allows to charge the next buckets earlier. When using the same process conditions during the first 10 min of the process, the second bucket could be charged 3 min earlier than without the hot heel practice (Fig. 8a). The process time line in Figs. 5a and b was therefore shifted 3

min earlier just before the second bucket was added. The lime addition was lowered by about 200 kg to account for the lower amount of produced SiO<sub>2</sub> and maintain the same slag basicity. The advantage of such practice can be observed in the temperature profile during the first 10 min of the heat (Fig. 10b). The liquid metal temperature is much higher (> 1400 °C) and more stable than when a hot heel is not used (Fig. 7). With such process conditions, melting of the scrap is completed in 36 min (Fig. 10a) and end of refining is achieved at 41 min with endpoint values similar to those of the original simulation (Fig. 10b and c). Notably, the simulation in Fig. 10 is only illustrative and the process operating conditions may be further improved to take advantage of the melt conditions.

### SUMMARY

In the present study, a kinetic process model was developed for the EAF process based on the EERZ approach and accurate FactSage thermochemical databases. The EAF process was divided into ten reaction zones to account for the main process phenomena: heating of the charge by arc and burners, scrap melting, O<sub>2</sub> and C injection, flux dissolution, slag-metal-gas reactions and post-combustion. Empirical relations linked to process conditions and model parameters are employed to describe each reaction zone. Each type of scrap forming the scrap mix is treated individually to account for difference in melting behavior due to different size and composition. The model can predict the evolution of the mass, temperature and chemistry of the scrap, liquid metal, slag and gas phases based on industrial operation conditions and model parameters.

Input data and endpoint measurements from industrial EAFs were employed to determine the model parameters and validate the model. The simulation results of a published industrial EAF show very good agreement with the measured endpoint composition and temperature of the liquid metal and slag. The effect and benefit of a hot heel practice on scrap melting and process performance are illustrated using the present model. Such process models provide an essential tool to assist in the optimization of the process, design of the operation practices to improve the performance and competitiveness of the EAF.

The present EAF model can be used to simulate a wide range of operation conditions to generate simulated process data. Based on the simulated data, the level 2 model at the plant can be improved for more accurate control of EAF operation. As the present EAF process model can provide the simulation results within 1/5 to 1/10 of real EAF operation time even by using a conventional desktop computer, a real-time operation guidance in EAF operation rooms is also possible.

### ACKNOWLEDGEMENTS

Financial support from Tata Steel Europe, Posco, Hyundai Steel, Nucor Steel, RioTinto Iron and Titanium, Nippon Steel Corp., JFE Steel, Voestalpine, RHI Magnesita, SeAH Besteel, Doosan Heavy Industry and Construction, and SCHOTT AG is gratefully acknowledged. This work was also partially supported by the Korea Institute of Energy Technology Evaluation and Planning (KETEP) grant funded by the Korean government (MOTIE) (20217510100080, Development of critical metal recovery technologies (capacity of 200 kg/day) from low-grade solid wastes for the foundation of open access recycling platform).

### CONFLICT OF INTERESTS

The present author states that there is no conflict of interest.

### REFERENCES

1. J. Madias, *Treatise on Process Metallurgy - Volume 3: Industrial Processes*, ed. S. Seetharaman (Elsevier, Oxford, UK, ), pp. 271–300.
2. International Energy Agency, *Iron and Steel Technology Roadmap* (International Energy Agency, Paris, 2020).
3. H.J. Odenthal, A. Kemminger, F. Krause, L. Sankowski, N. Uebber, and N. Vogl, *Steel Res. Int.* 89, 1700098. (2018).
4. J.G. Bekker, I.K. Craig, and P.C. Pistorius, *ISIJ Int.* 39, 23–32. (1999).
5. R.D. Morales, H. Rodríguez-Hernández, and A.N. Conejo, *ISIJ Int.* 41, 426–435. (2001).
6. R.D. Morales, A.N. Conejo, and H.H. Rodriguez, *Metall. Mater. Trans. B* 33, 187–199. (2002).
7. R.D.M. MacRosty, and C.L.E. Swartz, *Ind. Eng. Chem. Res.* 44, 8067–8083. (2005).
8. H. Matsuura, C.P. Manning, R.A.F.O. Fortes, and R.J. Fruehan, *ISIJ Int.* 48, 1197–1205. (2008).
9. V. Logar, D. Dovžan, and I. Škrjanc, *ISIJ Int.* 52, 402–412. (2012).
10. V. Logar, D. Dovžan, and I. Škrjanc, *ISIJ Int.* 52, 413–423. (2012).
11. F. Opitz, and P. Treffinger, *Metall. Mater. Trans. B* 47, 1489–1503. (2016).
12. F. Opitz, P. Treffinger, and J. Wöllenstein, *Metall. Mater. Trans. B* 48, 3301–3315. (2017).
13. T. Meier, K. Gandt, T. Hay, and T. Echterhof, *Steel Res. Int.* 89, 1700487. (2018).
14. T. Hay, A. Reimann, and T. Echterhof, *Metall. Mater. Trans. B* 50, 2377–2388. (2019).
15. A. Fathi, Y. Saboohi, I. Škrjanc, and V. Logar, *Steel Res. Int.* 88, 1600083. (2017).
16. Y. Saboohi, A. Fathi, I. Škrjanc, and V. Logar, *IEEE Trans. Ind. Electron.* 66, 8030–8039. (2019).
17. T. Hay, V.V. Visuri, M. Aula, and T. Echterhof, *Steel Res. Int.* 92, 2000395. (2021).
18. M.A. Van Ende, Y.M. Kim, M.K. Cho, J. Choi, and I.H. Jung, *Metall. Mater. Trans. B* 42, 477–489. (2011).
19. E. Moosavi-Khoonsari, M.A. Van Ende and I.H. Jung, Kinetic model for hot metal pretreatment using lime and magnesium. *Paper presented at the ICS 2018 - 7th International Congress on Science and Technology of Steelmaking*, Venice, Italy, June 13-15 2018.
20. M.A. Van Ende, and I.H. Jung, *CAMP-ISIJ* 28, 527–530. (2015).
21. M.A. Van Ende and I.H. Jung, A kinetic BOF process simulation model. *Paper presented at the Asia Steel International Conference*, Yokohama, Japan, October 5–8 2015.

22. D. You, C. Bernhard, P. Mayer, J. Fasching, G. Kloesch, R. Rössler, and R. Ammer, *Metall. Mater. Trans. B* 52, 1854–1865. (2021).
23. M.A. Van Ende, and I.H. Jung, *ISIJ Int.* 54, 489–495. (2014).
24. M.A. Van Ende, and I.H. Jung, *Metall. Mater. Trans. B* 48, 28–36. (2017).
25. I.H. Jung, and M.A. Van Ende, *Metall. Mater. Trans. B* 51, 1851–1874. (2020).
26. D. Kumar, K.C. Ahlborg, and P.C. Pistorius, *Metall. Mater. Trans. B* 50, 2163–2174. (2019).
27. D. You, S.K. Michelic, and C. Bernhard, *Steel Res. Int.* 91, 2000045. (2020).
28. Y. Ren, L. Zhang, H. Ling, Y. Wang, D. Pan, Q. Ren, and X. Wang, *Metall. Mater. Trans. B* 48, 1433–1438. (2017).
29. S.P.T. Piva, D. Kumar, and P.C. Pistorius, *Metall. Mater. Trans. B* 48, 37–45. (2017).
30. J.H. Shin, Y. Chung, and J.H. Park, *Metall. Mater. Trans. B* 48, 46–59. (2017).
31. C. Xuan, E.S. Persson, J. Jensen, R. Sevastopolev, and M. Nzotta, *J. Alloys Compd.* 812, 152149. (2020).
32. C.W. Bale, E. Bélisle, P. Chartrand, S.A. Deckerov, G. Eriksson, A.E. Gheribi, K. Hack, I.H. Jung, Y.B. Kang, J. Melançon, A.D. Pelton, S. Petersen, C. Robelin, J. Sangster, P. Spencer, and M.A. Van Ende, *Calphad* 54, 35–53. (2016).
33. S. Petersen, and K. Hack, *Int. J. Mat. Res.* 98, 935–945. (2007).
34. H. Gaye, M. Wanin, P. Gugliermi and P. Schittly, Kinetics of scrap dissolution in the converter, theoretical model and plant experimentation. *Paper presented at the Steelmaking Conference Proceedings*, Detroit, MI, April 14–17 1985.
35. D.A. Goldstein, and R.J. Fruehan, *Metall. Mater. Trans. B* 30, 945–956. (1999).
36. G.H. Li, B. Wang, Q. Liu, X.Z. Tian, R. Zhu, L.N. Hu, and G.G. Cheng, *Int. J. Miner. Metall. Mater.* 17, 715–722. (2010).
37. N. Dogan, G.A. Brooks, and M.A. Rhamdhani, *ISIJ Int.* 51, 1102–1109. (2011).
38. J. Peter, K.D. Peaslee, D.G.C. Robertson and B.G. Thomas, Experimental study of kinetic processes during the steel treatment at two LMF's. Paper presented at the AISTech 2005, Charlotte, N.C., May 9–12 2005.
39. K.J. Graham, and G.A. Irons, *Iron Steel Technol.* 6, 164–173. (2009).
40. A. Harada, N. Maruoka, H. Shibata, and S.Y. Kitamura, *ISIJ Int.* 53, 2110–2117. (2013).
41. J. Li, G. Brooks, and N. Provatas, *Metall. Mater. Trans. B* 36, 293–302. (2005).
42. R. Inoue, and H. Suito, *ISIJ Int.* 46, 174–179. (2006).
43. F. Pahlevani, K. Shinya, H. Shibata, and N. Maruoka, *ISIJ Int.* 50, 822–829. (2010).

**Publisher's Note** Springer Nature remains neutral with regard to jurisdictional claims in published maps and institutional affiliations.